

# All-electrostatic valley qubit gates in tilted Dirac-Weyl semimetals

Can Yesilyurt<sup>1,\*</sup>

<sup>1</sup>Nanoelectronics Research Center, Istanbul, Turkey

\*Correspondence: can@nanorescenter.com, can-yesilyurt@hotmail.com

March 2026

## Abstract

Valley degrees of freedom in tilted Dirac materials offer a route toward fully electrical quantum control, but previous electrostatic barrier schemes have used the valley index only as a classical filtering resource. Here, we show that a smooth electrostatic barrier operated in a quantum point contact geometry at normal incidence instead realizes coherent valley phase control. In the single-mode regime, both valleys retain near-unit transmission while the tilt-induced valley-dependent traversal phase generates a controllable relative phase shift  $\Delta\delta = \delta_K - \delta_{K'}$  between the  $|K\rangle$  and  $|K'\rangle$  components of the wavefunction. The resulting electrostatic element implements a tunable valley  $Z$  rotation whose accessible phase range covers 99.5% of the full  $2\pi$  interval while maintaining a transmission-balance metric  $\mathcal{B}$  above 0.99 over a broad parameter window. Combined with a fixed valley-mixing element that supplies an  $X$  rotation, this enables universal single-qubit control through a  $Z$ - $X$ - $Z$  Euler decomposition. For realistic parameters, the ballistic gate time is  $\sim 50$  fs, with particularly favourable operating windows in 8- $Pmmn$  borophene and  $\text{WTe}_2$ . These results establish tilted Dirac semimetals as a platform for coherent, all-electrical valley manipulation.

# Introduction

The valley index  $\tau = \pm 1$  labelling the inequivalent  $K$  and  $K'$  Dirac points in momentum space provides a binary quantum number analogous to spin, and has attracted intense interest as a carrier of quantum information [1–5]. Manipulating valley states with the speed and tunability available to charge-based devices would combine the topological robustness of the valley degree of freedom with all-electrical control [6–8]. Valley-polarized currents have been generated using magnetic barriers [9–11], strain engineering [12–15], optical pumping [4, 16, 17], and line defects [18], but each approach introduces fabrication or operational constraints that limit scalability. Magnetic barriers reduce practicability and add fabrication complexity, strain engineering demands nanoscale mechanical control, and optical schemes preclude device-level integration.

A qualitatively different avenue has opened with the recognition that electrostatic barriers on tilted Dirac materials can produce valley-dependent tunnelling without any external symmetry-breaking field [6, 19–21, 24, 25]. In these systems, the low-energy Hamiltonian contains a tilt term that breaks particle-hole symmetry, with the tilt direction reversing between opposite valleys [22, 23]. When carriers scatter from an electrostatic barrier, this valley-dependent anisotropy produces distinct transmission profiles  $T_K(\theta) \neq T_{K'}(\theta)$  [6, 8, 24]. It has recently been demonstrated that a single electrostatic barrier rotated by an angle  $\phi$  relative to the transport direction produces finite valley-polarized conductance, and that the scattering problem at a smooth barrier interface maps analytically onto the parabolic cylinder equation [19, 26, 27]. These advances, however, have treated the valley degree of freedom as a *classical* filter — characterizing the effect through conductance polarization, which averages over all transverse modes and discards the quantum phase information. The question of whether the same electrostatic mechanism can perform coherent, unitary rotations on a valley qubit state has not been addressed.

Here, we show that smooth electrostatic barriers on tilted Dirac semimetals, operated in a single-mode quantum point contact (QPC) geometry, realize electrically tunable valley

phase gates. The essential insight is that the regime which maximizes coherent phase control is complementary to the regime that maximizes valley filtering: the valley filter operates in a wide channel where many modes contribute to the integrated conductance, whereas the phase gate operates in a single-mode QPC near normal incidence, where both valleys transmit with near-unit probability but acquire distinct phases. We map the full parameter space of this phase gate, demonstrate that the achievable  $Z$ -rotation range covers 99.5% of  $2\pi$  at high transmission balance, and show that a  $Z$ - $X$ - $Z$  Euler decomposition provides universal single-qubit control for candidate tilted Dirac materials.

## Results

### Smooth barrier as a valley phase gate

The mechanism underlying the valley phase gate is illustrated in Fig. 1. A smooth barrier (Fig. 1a) of width  $d$  and height  $V_0$ , rotated by angle  $\phi$  with respect to the transport direction, decomposes the tilt vector into perpendicular and parallel components in the barrier frame:  $t_{\perp} = \tau t \sin \phi$  and  $t_{\parallel} = \tau t \cos \phi$ , where  $\tau = \pm 1$  is the valley index [26]. When a carrier at normal incidence ( $k_y = 0$ ) traverses such a barrier, both valleys retain near-unit transmission in the smooth-barrier regime [23, 27], so the barrier is effectively transparent in amplitude (Fig. 1b). The transmission *phases*, however, differ: the valley-dependent perpendicular wavevector  $k_{\perp}^{(\tau)}$  inside the barrier, which is obtained from the tilted dispersion relation (see Methods), accumulates a valley-dependent propagation phase  $\delta_{\tau} = \int k_{\perp}^{(\tau)} dx$ , yielding a relative phase shift

$$\Delta\delta = \delta_K - \delta_{K'} \neq 0 \tag{1}$$

that is continuously tunable via the gate voltage  $V_0$  (Fig. 1c).

The smooth barrier profile is critical to achieving coherent phase control. A sharp barrier supports Fabry-Pérot resonances—multiple reflections between the two abrupt interfaces—

whose resonance conditions depend on the valley index through  $t_{\parallel}$ . These resonances modulate the transmission *amplitudes*  $|t_K|$  and  $|t_{K'}|$  differently, producing valley-asymmetric amplitude oscillations that spoil the unitary character of the gate (Fig. 1d, dashed red curve). A smooth barrier ( $\sigma \gtrsim 5$  nm) suppresses these reflections, yielding near-equal transmission amplitudes for both valleys over a broad voltage range. To quantify this, we define the transmission-balance metric

$$\mathcal{B} = \frac{\min(T_K, T_{K'})}{\max(T_K, T_{K'})}, \quad (2)$$

where  $T_{\tau} = |t_{\tau}|^2$ . The green-shaded region in Fig. 1d marks the operating window where  $\mathcal{B} > 0.99$  for  $\sigma = 10$  nm. We emphasize that  $\mathcal{B}$  is an amplitude-balance proxy, not a full quantum gate fidelity; it isolates the regime in which the dominant valley-selective action is phase accumulation rather than probability filtering. A full gate-fidelity assessment would additionally require characterization of decoherence, higher-mode leakage, and state-preparation errors, which lie beyond the scope of the present work.

The analytical structure of the valley phase shift can be understood from the connection to the parabolic cylinder equation established in the companion manuscript [26]. At normal incidence, the effective Weber index  $n = -k_y^2 \ell^2 / (1 - t_{\perp}^2)$  vanishes, placing the carrier at the centre of the tunnelling envelope where transmission is maximal. The phase accumulated during traversal depends on  $k_{\perp}^{(\tau)}$ , which differs between valleys because the tilt decomposition  $t_{\perp} = \tau t \sin \phi$  reverses sign. Figure 1e compares the numerically computed  $\Delta\delta$  with an analytical estimate based on the valley-dependent  $k_{\perp}$  difference inside the barrier, confirming that the phase shift originates from the tilt-induced wavevector splitting. In the valley birefringent regime ( $V_0 < E_F$ ), where no hole pocket forms inside the barrier, the phase accumulates linearly with barrier width  $d$  at near-unit transmission balance (Fig. 1f), providing a particularly clean operating window for precision gate calibration.

## Qubit subspace and coherence assumptions

The qubit interpretation of the valley phase gate rests on a set of physical assumptions that define the regime of validity. We require: (i) a QPC-defined single transverse mode centred at  $k_y \approx 0$ , ensuring that the carrier occupies a well-defined point in the angular transmission landscape; (ii) coherent ballistic propagation across the gated region, so that the complex transmission amplitudes retain their phases; (iii) negligible intervalley scattering within each smooth-barrier segment, preserving the valley index as a good quantum number during traversal; and (iv) negligible leakage into higher transverse modes, maintaining the two-dimensional valley Hilbert space.

Under these conditions, a carrier injected as the superposition  $|\psi\rangle = \alpha|K\rangle + \beta|K'\rangle$  remains within the valley subspace while traversing the barrier. The outgoing state is  $|\psi'\rangle = t_K\alpha|K\rangle + t_{K'}\beta|K'\rangle$ , with  $t_\tau = |t_\tau|e^{i\delta_\tau}$ . In the high-balance regime ( $\mathcal{B} \approx 1$ ), the amplitudes  $|t_K| \approx |t_{K'}| \approx 1$  and the operation reduces, up to a global phase, to a  $Z$  rotation on the valley Bloch sphere:

$$R_z(\Delta\delta) = \begin{pmatrix} e^{-i\Delta\delta/2} & 0 \\ 0 & e^{i\Delta\delta/2} \end{pmatrix}. \quad (3)$$

## Phase gate parameter space

The parameter space for the valley  $Z$  gate is mapped comprehensively in Fig. 2. The two-dimensional phase landscape  $\Delta\delta(\sigma, V_0)$  at normal incidence (Fig. 2a) reveals a sharp dichotomy between the smooth- and sharp-barrier regimes. Smooth barriers ( $\sigma \gtrsim 5$  nm) produce a monotonically varying phase that spans the full  $[-\pi, \pi]$  range as  $V_0$  is swept from below  $E_F$  through the  $n$ - $p$ - $n$  transition, whereas sharp barriers ( $\sigma \lesssim 1$  nm) exhibit rapid oscillatory structure arising from Fabry-Pérot resonances cycling through constructive and destructive conditions. The corresponding transmission-balance map  $\mathcal{B}(\sigma, V_0)$  (Fig. 2b) confirms that near-unit balance is achieved throughout the smooth-barrier regime, with the contour  $\mathcal{B} = 0.99$  enclosing a large, connected region of parameter space. Dashed contours

of  $|\Delta\delta|$  overlaid on the balance map show that substantial phase shifts ( $|\Delta\delta| > 1$  rad) co-exist with high transmission balance — the two requirements are not in tension for smooth barriers.

Figures 2c,d show the dependence of  $\Delta\delta$  and  $\mathcal{B}$  on the barrier rotation angle  $\phi$  for several tilt values. The phase difference increases with both  $t$  and  $\phi$ , as expected from the larger tilt decomposition  $t_{\perp} = \tau t \sin \phi$  at larger angles. The transmission balance remains near unity for  $\phi \lesssim 30^{\circ}$  at all tilt values shown ( $t = 0.2\text{--}0.7$ ), dropping sharply only at large angles where the perpendicular tilt component approaches the type-II boundary. This defines a broad operating window in the  $(t, \phi)$  plane where the smooth barrier acts as a high-quality phase gate.

The dependence on barrier width  $d$  is shown in Fig. 2e for three barrier heights. In the  $n$ - $p$ - $n$  regime ( $V_0 > E_F$ ), the phase oscillates with  $d$  due to residual Fabry-Pérot structure inside the barrier, while in the birefringent regime ( $V_0 < E_F$ ), the phase accumulates monotonically with  $d$ , consistent with the absence of a hole pocket. The comprehensive phase diagram  $\Delta\delta(t, \phi)$  in Fig. 2f, with transmission-balance contours overlaid, provides a design chart for selecting material and geometry parameters. The contour  $\mathcal{B} = 0.99$  (solid black) encloses most of the moderate-tilt, moderate-angle parameter space, confirming that the phase gate is robust across a wide range of experimentally relevant conditions.

Quantitatively, the achievable phase range at  $\mathcal{B} > 0.99$  is  $\Delta\delta \in [-3.13, 3.12]$  rad, corresponding to 99.5% of the full  $2\pi$   $Z$ -rotation. This near-complete  $Z$ -gate range is the central numerical result of this work.

## Universal single-qubit control

Universal single-qubit control requires, in addition to the  $Z$ -rotation, a rotation about a non-parallel axis [28]. In the valley qubit architecture, this is provided by any element that coherently couples  $|K\rangle$  and  $|K'\rangle$ , realizing an  $R_x(\beta)$  rotation. Physical implementations include engineered short-range scatterers, zigzag-edge constrictions, or other intervalley-

coupling nanostructures [1, 18]; the specific mechanism is not critical, as only a single fixed  $\beta$  is needed. The resulting  $Z$ - $X$ - $Z$  Euler decomposition

$$U(\alpha, \beta, \gamma) = R_z(\alpha) \cdot R_x(\beta) \cdot R_z(\gamma), \quad (4)$$

where both  $R_z$  gates are independently voltage-tunable smooth barriers, generates any target unitary in  $SU(2)$  when  $\beta = \pi/2$  and  $\alpha, \gamma$  each span  $[0, 2\pi]$  [28].

The Bloch-sphere trajectories in Fig. 3a demonstrate the  $Z$ -gate action: sweeping  $V_0$  traces equatorial arcs on the Bloch sphere for two different input states, confirming that the voltage-controlled phase shift produces the expected rotation around the  $z$ -axis. Figure 3b shows the full  $Z$ - $X$ - $Z$  protocol applied to the input  $|K\rangle$ : the dense teal dots, obtained by sweeping  $\alpha, \gamma \in [0, 2\pi]$  with  $\beta = \pi/2$ , uniformly cover the entire Bloch sphere, demonstrating that every single-qubit state is reachable. Coloured trajectories highlight the three-step gate paths to four representative target states.

The device architecture implementing this protocol is shown in Fig. 3c. A QPC-defined single-mode channel hosts two independently gated smooth barriers, providing  $R_z(\alpha)$  and  $R_z(\gamma)$ , separated by a fixed valley-mixing element providing  $R_x(\beta)$ . The source QPC prepares a single transverse mode at  $k_y \approx 0$ ; the drain QPC reads out the valley state. The gate voltages  $V_1$  and  $V_2$  are the only tunable parameters, with the barrier angle  $\phi$  and width  $d$  set lithographically.

## Material candidates and operating regimes

The valley phase gate mechanism applies to any two-dimensional material hosting tilted Dirac or Weyl cones with valley-dependent tilt orientations. Figure 4a maps the valley phase shift as a function of tilt parameter, with three candidate platforms marked.

8- $Pmmn$  borophene ( $t \approx 0.46$ ,  $v_F \approx 0.86 \times 10^6$  m/s) [29, 30] provides a large phase shift ( $|\Delta\delta| = 3.03$  rad at  $V_0 = 150$  meV) at high transmission balance, with the tilt direction and

valley structure precisely matching the model assumptions. The Dirac fermion character of this polymorph has been confirmed experimentally [31], and the tilt can in principle be tuned by atomic substitutions [32], allowing traversal of the phase diagram along the tilt axis. A key experimental challenge remains the large-area synthesis of 8-*Pmmn* borophene on suitable substrates.

WTe<sub>2</sub> ( $t \approx 0.35$ ) [34, 35, 37] offers the most accessible experimental platform. Gate-tunable transport at room temperature has been demonstrated [33], and the required angled-gate geometry is compatible with standard electron-beam lithography. The moderate tilt places WTe<sub>2</sub> in the monotonic-phase regime where the transmission balance remains high and the phase varies smoothly with  $V_0$ .

The organic conductor  $\alpha$ -(BEDT-TTF)<sub>2</sub>I<sub>3</sub> ( $t \approx 0.72$ ) [22, 36] provides a continuously pressure-tunable tilt, enabling systematic exploration of the phase diagram, though its lower Fermi velocity ( $v_F \sim 10^4$ – $10^5$  m/s) requires proportionally wider barriers or larger gate voltages.

The gate operates at the ballistic traversal time  $\tau_{\text{gate}} = d/v_F \approx 50$  fs for  $d = 50$  nm (Fig. 4c), which is three to four orders of magnitude faster than typical spin-qubit gate times. Whether this speed advantage can be exploited depends on the valley decoherence time  $T_2$ , which is governed by intervalley scattering from short-range disorder. In clean WTe<sub>2</sub>, where ballistic transport has been established at room temperature [33, 34], estimated decoherence times of  $T_2 \sim 10$  ps would permit  $\sim 200$  gate operations per coherence window (Fig. 4d), approaching the threshold for fault-tolerant quantum error correction. For 8-*Pmmn* borophene, shorter estimated mean free paths suggest  $T_2 \sim 1$  ps, yielding  $\sim 20$  operations per coherence time. These are order-of-magnitude estimates; experimental determination of valley-resolved decoherence in these materials remains an open challenge.

The operating regime map in Fig. 4b clarifies the distinction between the quantum phase-gate regime and the classical valley-filter regime. At low conductance polarization  $|\mathcal{P}|$  and high  $|\Delta\delta|$ , the system operates as a coherent phase gate with high transmission balance

(green points). At large  $|\mathcal{P}|$  and low  $|\Delta\delta|$ , the barrier acts as a classical valley filter with strongly asymmetric transmission (red points). The two regimes are complementary: the classical filter, realized in a wide-channel geometry, produces valley-polarized currents for state preparation and readout [19, 26], while the phase gate, realized in a QPC geometry at normal incidence, performs coherent unitary rotations. A complete valley qubit architecture would use both modes of operation.

## Discussion

The results presented here establish that smooth electrostatic barriers in tilted Dirac semimetals, operated in a single-mode geometry, realize electrically tunable valley phase gates with high transmission balance and femtosecond gate times. The mechanism exploits the same valley-dependent Klein tunnelling physics that underlies the classical valley filter [19] and the parabolic-cylinder analytical framework [26], but in a fundamentally different operating regime where the quantum phase, rather than the transmission probability, carries the information.

Several aspects of the proposal merit further discussion. First, the transmission-balance metric  $\mathcal{B}$  provides a necessary but not sufficient condition for high-quality gate operation. A full characterization of the gate error budget would require accounting for decoherence during traversal, dephasing in the free-propagation regions between barriers, finite-temperature effects, and imperfections in the QPC mode selection. Each of these contributions is material-dependent and will ultimately need to be assessed experimentally. The present work identifies the operating regime in which the *intrinsic* barrier physics supports coherent phase control; whether that regime is experimentally accessible in specific materials is a question that the transmission-balance analysis alone cannot answer.

Second, the  $R_x$  valley-mixing element has been treated as a generic component supplying a fixed rotation. The fidelity of the full  $Z$ - $X$ - $Z$  gate sequence depends sensitively on the

coherence of this element. Several physical mechanisms for intervalley coupling are known [1, 18], but quantifying their coherence properties in the context of a qubit gate protocol is an important open problem.

Third, the comparison with other qubit platforms should be made with appropriate caveats. The 50 fs gate time is a ballistic traversal estimate that does not include the settling time of the gate voltage, which in practice would be limited by the  $RC$  time constant of the electrostatic gate circuit ( $\sim 1$ – $10$  ps for optimized nanostructures). Even including this overhead, the total gate cycle remains in the picosecond range, which is competitive with the fastest solid-state qubit platforms.

Finally, the framework developed here is not specific to valley qubits in tilted Dirac materials. The core principle—that a smooth potential barrier can impart a species-dependent phase at near-unit transmission—applies to any system where two internal degrees of freedom experience different effective potentials during tunnelling. Analogous phase gates may be realizable for spin, sublattice, or layer pseudospin degrees of freedom in other two-dimensional materials, broadening the potential impact of this approach.

In summary, the  $Z$ – $X$ – $Z$  architecture provides a concrete route to universal single-valley-qubit control using only gate voltages and device geometry, with no magnetic fields, strain, or optical excitation. The all-electrical nature of the control, the ultrafast gate times, and the compatibility with lithographic fabrication position valley qubits in tilted Dirac materials as a platform worthy of experimental investigation for coherent quantum information processing.

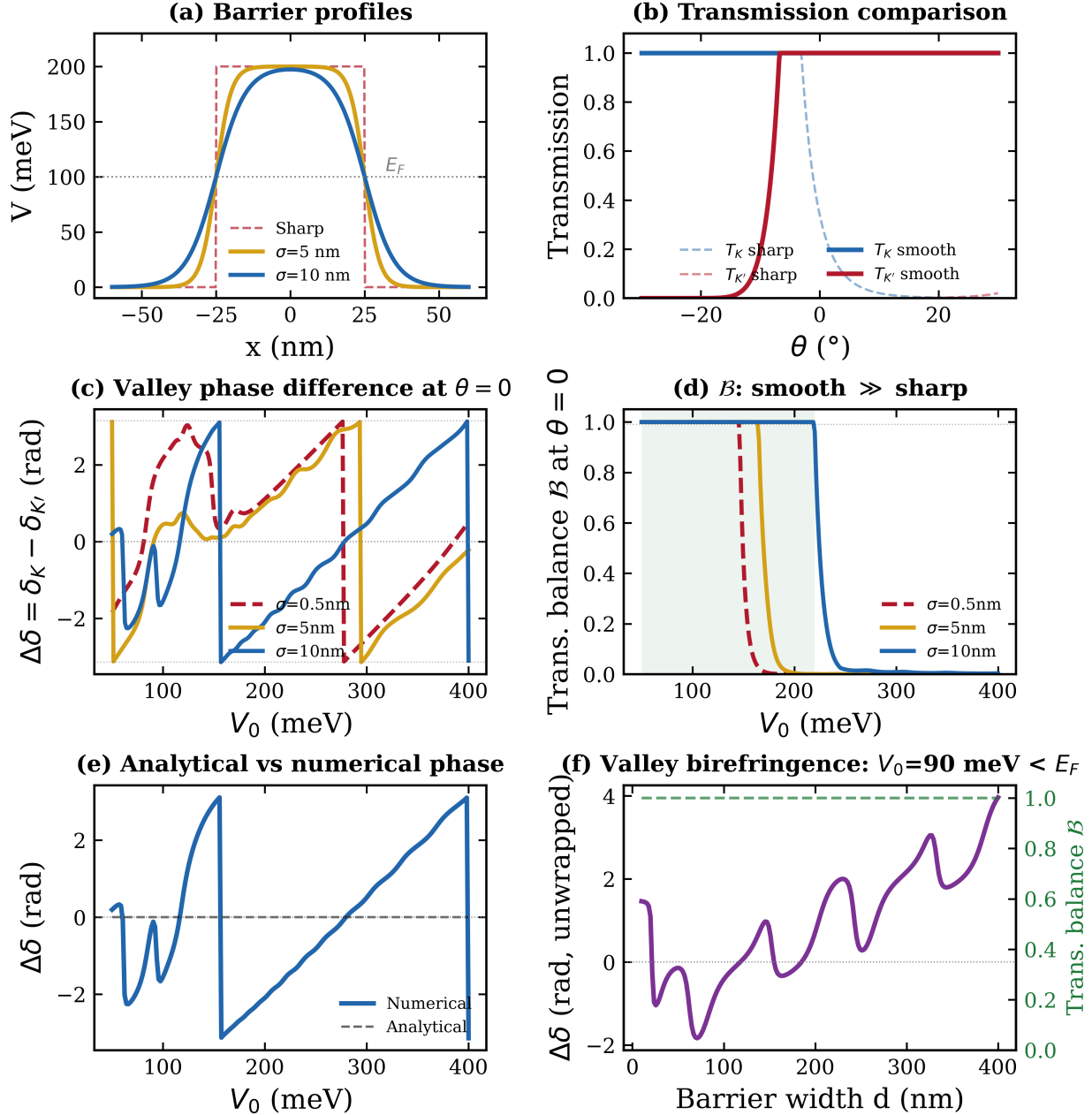


Figure 1: **Smooth electrostatic barrier as a valley phase gate.** **a**, Barrier potential

profiles: sharp (dashed red),  $\sigma = 5$  nm (gold), and  $\sigma = 10$  nm (blue) for a barrier of width  $d = 50$  nm and height  $V_0 = 200$  meV. The Fermi energy  $E_F = 100$  meV is indicated. **b**,

Valley-resolved transmission  $T(\theta)$  comparing sharp (dashed) and smooth ( $\sigma = 10$  nm, solid) barriers at tilt  $t = 0.5$  and barrier rotation  $\phi = 20^\circ$ . The smooth barrier suppresses the Fabry-Pérot oscillations that produce valley-asymmetric amplitude modulation. **c**,

Valley phase difference  $\Delta\delta = \delta_K - \delta_{K'}$  at normal incidence ( $\theta = 0$ ) as a function of  $V_0$  for three barrier smoothness values. The smooth barrier ( $\sigma = 10$  nm) produces a monotonic, continuously tunable phase spanning the full  $[-\pi, \pi]$  range. **d**,

Transmission-balance metric  $\mathcal{B} = \min(T_K, T_{K'}) / \max(T_K, T_{K'})$  at  $\theta = 0$ . The green-shaded region indicates  $\mathcal{B} > 0.99$  for  $\sigma = 10$  nm, demonstrating near-equal transmission amplitudes over a broad voltage range. **e**,

Comparison of the numerical phase with the analytical estimate based on the valley-dependent  $k_\perp$  difference inside the barrier. **f**, Valley birefringent regime ( $V_0 = 90$  meV  $< E_F$ ):

the phase accumulates with barrier width  $d$  at near-unit transmission balance (dashed green), enabling precision phase calibration.

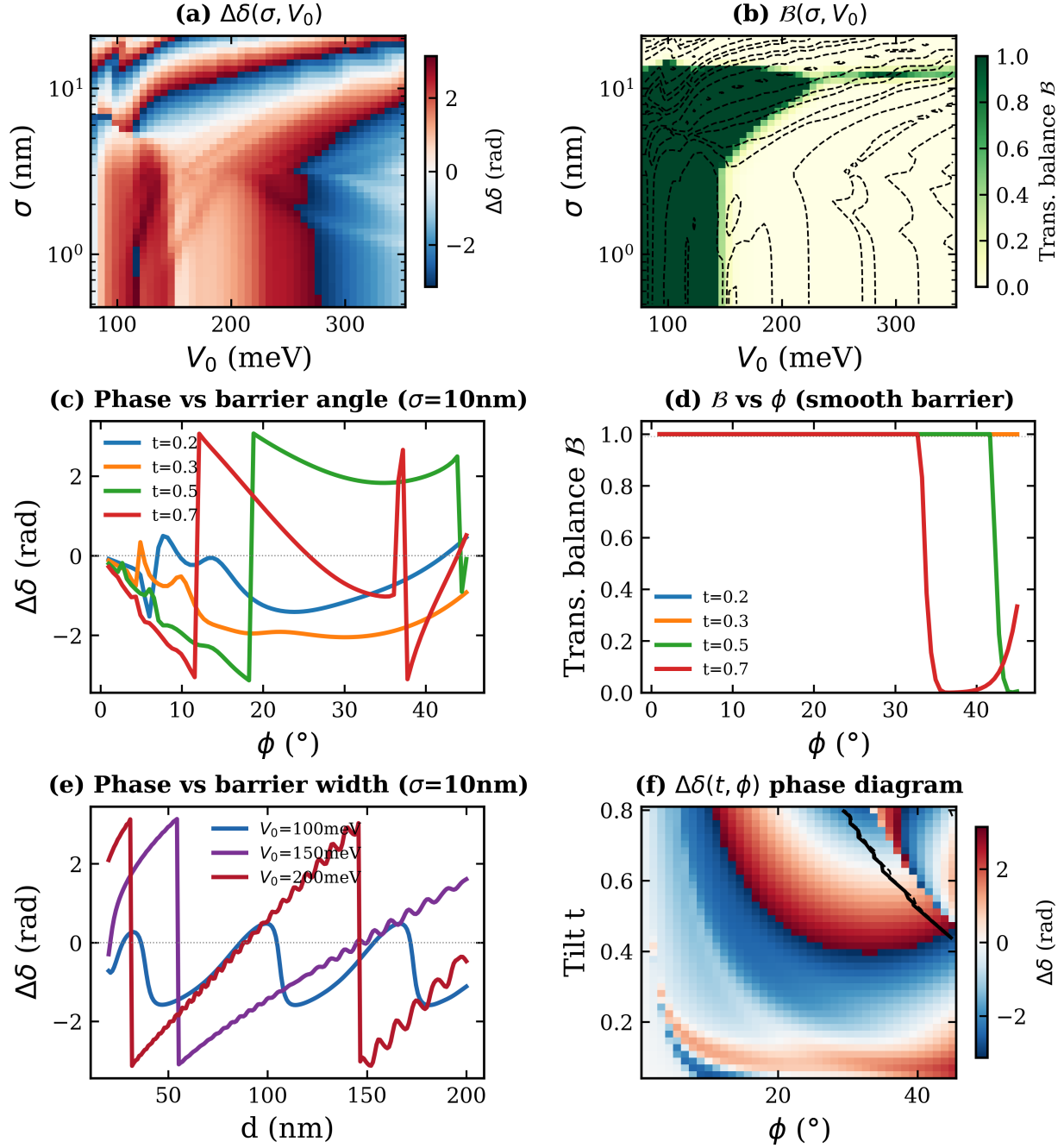


Figure 2: **Phase gate parameter space.** **a**, Valley phase difference  $\Delta\delta(\sigma, V_0)$  at normal incidence for  $t = 0.5$ ,  $\phi = 20^\circ$ ,  $d = 50$  nm. Smooth barriers ( $\sigma \gtrsim 5$  nm) yield monotonic, broadband phase control; sharp barriers produce oscillatory structure. **b**, Transmission-balance metric  $\mathcal{B}(\sigma, V_0)$ . Dashed contours show  $|\Delta\delta|$  levels. High transmission balance (dark green) occupies the entire smooth-barrier regime. **c**,  $\Delta\delta$  versus barrier rotation angle  $\phi$  for  $\sigma = 10$  nm,  $V_0 = 150$  meV at four tilt values. The phase increases with both  $t$  and  $\phi$ . **d**, Transmission balance versus  $\phi$ :  $\mathcal{B}$  remains near unity for  $\phi \lesssim 30^\circ$  at all tilts shown. **e**,  $\Delta\delta$  versus barrier width  $d$  for three barrier heights, showing phase accumulation with propagation distance. **f**, Phase diagram  $\Delta\delta(t, \phi)$  with transmission-balance contours (black curves:  $\mathcal{B} = 0.90$  dashed,  $\mathcal{B} = 0.99$  solid). The high-balance region covers most of the moderate-tilt, moderate-angle parameter space.

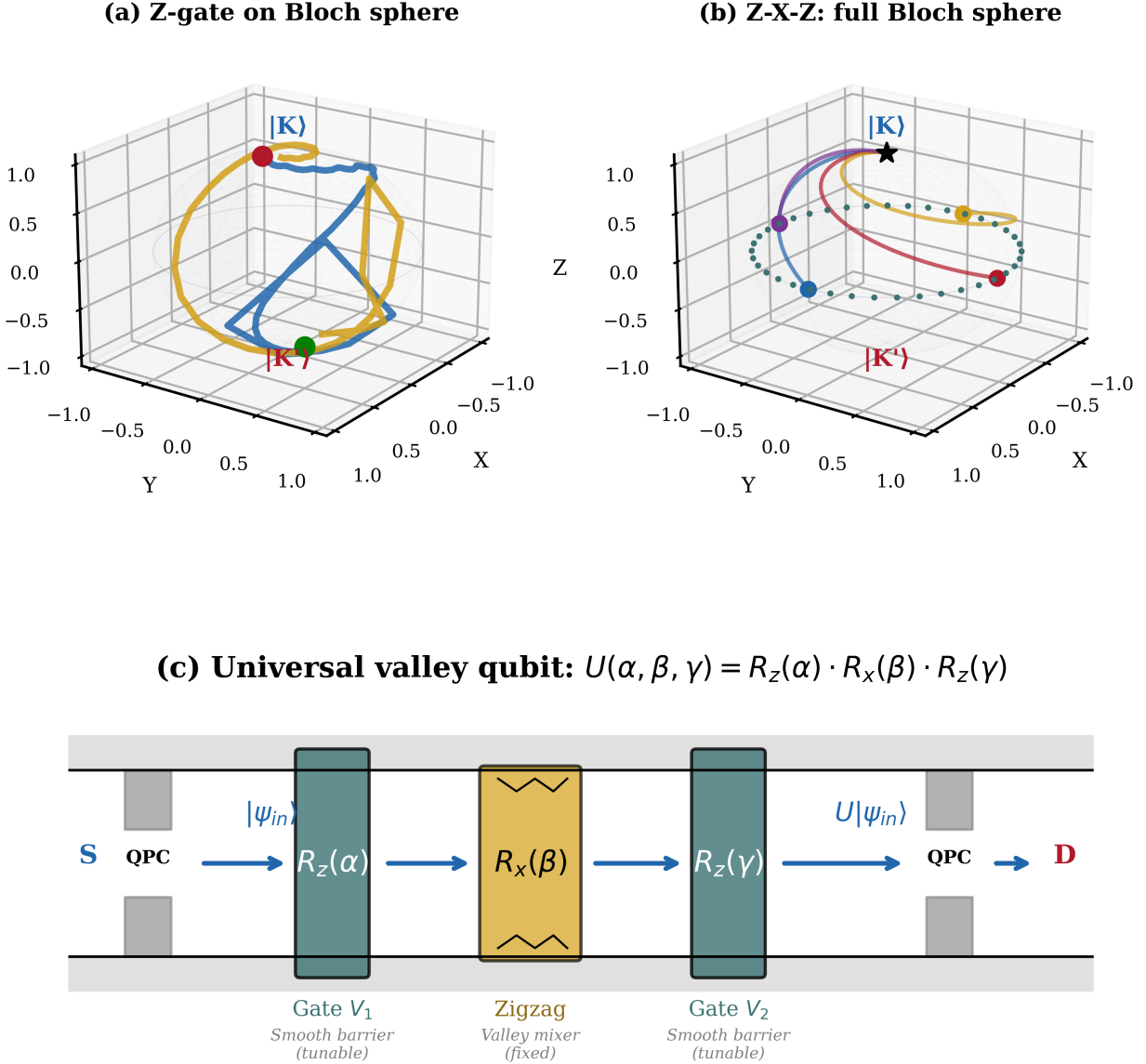


Figure 3: **Universal single-qubit gate via  $Z$ - $X$ - $Z$  Euler decomposition.** **a**, Bloch sphere trajectories under  $Z$ -gate operation: sweeping  $V_0$  traces arcs on the Bloch sphere for two different input states  $|\psi_{\text{in}}\rangle$ . Green and red dots mark the start and end points. **b**, Full Bloch-sphere coverage achieved by the  $Z$ - $X$ - $Z$  protocol  $U(\alpha, \beta, \gamma) = R_z(\alpha) \cdot R_x(\pi/2) \cdot R_z(\gamma)$  applied to  $|K\rangle$  (black star). Coloured trajectories show the three-step paths to four target states; teal dots show the dense sampling of the reachable state space. **c**, Device architecture: a QPC-defined single-mode channel with two independently gated smooth barriers (tunable  $V_1, V_2$ ) providing  $R_z(\alpha)$  and  $R_z(\gamma)$ , separated by a fixed valley-mixing element providing  $R_x(\beta)$ .

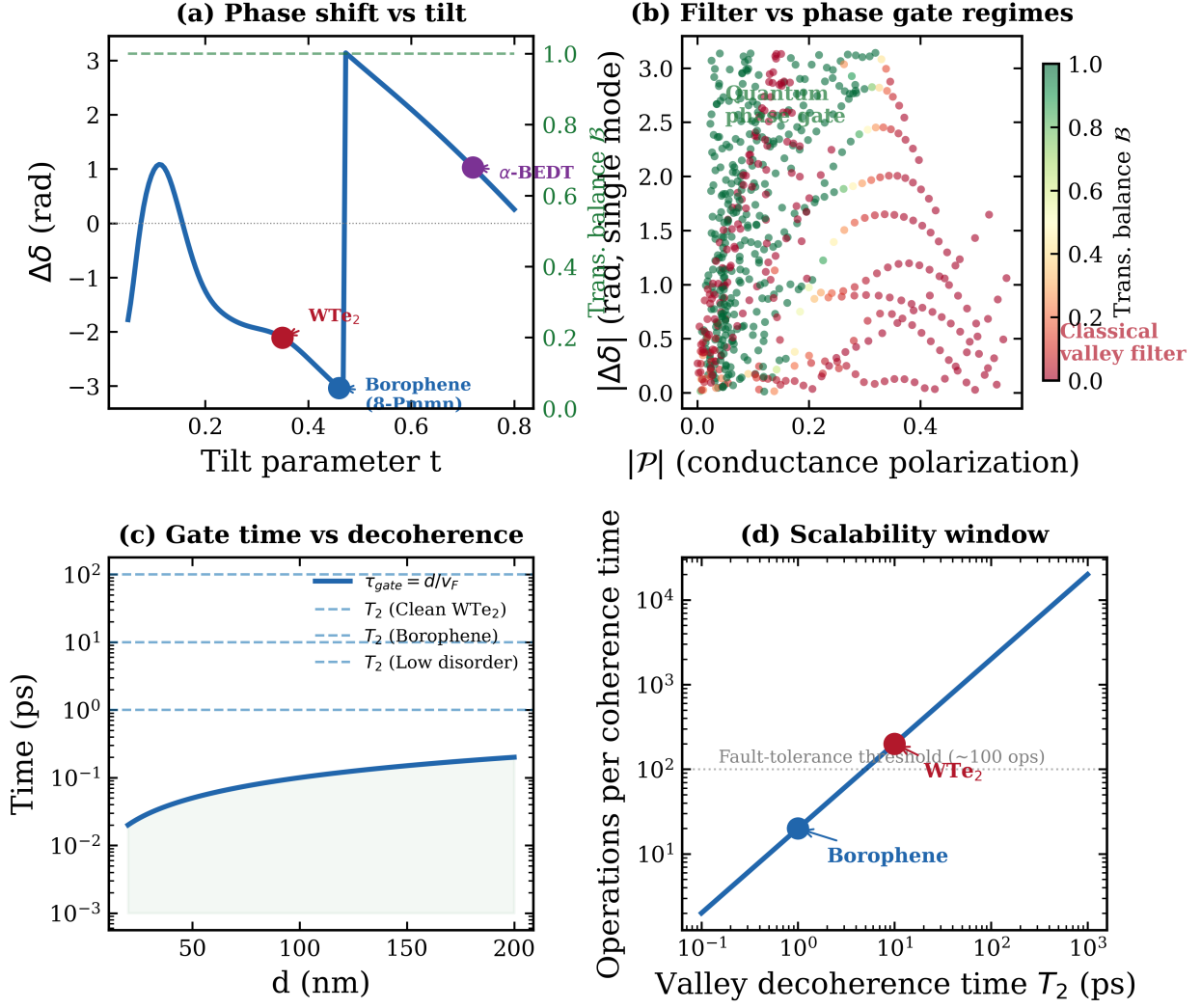


Figure 4: **Material candidates and operating regimes.** **a**, Valley phase shift  $\Delta\delta$  versus tilt parameter  $t$  at  $V_0 = 150$  meV,  $\sigma = 10$  nm,  $d = 50$  nm,  $\phi = 20^\circ$ . Material candidates are marked:  $8\text{-}Pmmn$  borophene ( $t = 0.46$ ),  $\text{WTe}_2$  ( $t = 0.35$ ),  $\alpha\text{-}(\text{BEDT-TTF})_2\text{I}_3$  ( $t = 0.72$ ). The right axis shows the transmission-balance metric (dashed green), which remains near unity throughout. **b**, Operating regime map: valley conductance polarization  $|\mathcal{P}|$  versus single-mode phase  $|\Delta\delta|$ , coloured by transmission balance  $\mathcal{B}$ . The quantum phase-gate regime (upper left, high  $\mathcal{B}$ ) is distinct from the classical valley-filter regime (lower right, low  $\mathcal{B}$ ). **c**, Gate time  $\tau_{\text{gate}} = d/v_F$  compared with estimated valley decoherence times  $T_2$  for different material platforms. **d**, Number of gate operations per coherence time  $T_2/\tau_{\text{gate}}$  as a function of  $T_2$ , with material estimates marked. The dotted line indicates the approximate fault-tolerance threshold ( $\sim 100$  operations).

# Methods

## Tilted Dirac Hamiltonian and barrier frame decomposition

The low-energy quasiparticles near a single Dirac point in a tilted two-dimensional material are described by the Hamiltonian

$$\hat{H} = \hbar v_F(\hat{k}_x\sigma_x + \hat{k}_y\sigma_y) + \hbar v_t\hat{k}_y\sigma_0 + V(x), \quad (5)$$

where  $v_F$  is the Fermi velocity,  $v_t = t \cdot v_F$  is the tilt velocity with dimensionless tilt parameter  $t$  ( $|t| < 1$  for type-I),  $\sigma_{x,y}$  are Pauli matrices,  $\sigma_0$  is the identity, and  $V(x)$  is an electrostatic potential [20–22]. The tilt is oriented along  $y$  and reverses sign between valleys:  $v_t \rightarrow \tau v_t$ , where  $\tau = +1$  ( $K$ ) and  $\tau = -1$  ( $K'$ ) [6, 24]. The energy dispersion with  $V = 0$  reads  $E = \hbar v_t k_y \pm \hbar v_F \sqrt{k_x^2 + k_y^2}$ , describing a Dirac cone tilted along  $k_y$ .

When the electrostatic barrier is rotated by angle  $\phi$  relative to the  $y$ -axis (barrier normal at angle  $\phi$  from  $x$ ), the tilt decomposes in the barrier frame as  $t_\perp = \tau t \sin \phi$  (perpendicular to the barrier) and  $t_\parallel = \tau t \cos \phi$  (parallel to the barrier). The conserved barrier-frame momentum is  $k_\parallel = -k_x \sin \phi + k_y \cos \phi$ , which depends nonlinearly on the laboratory-frame transverse momentum  $k_y$  through  $k_x = \sqrt{k_F^2 - k_y^2}$ .

## Smooth barrier transfer matrix

The smooth barrier potential is modelled as

$$V(x) = \frac{V_0}{2} \left[ \tanh\left(\frac{x + d/2}{\sigma}\right) - \tanh\left(\frac{x - d/2}{\sigma}\right) \right], \quad (6)$$

where  $d$  is the barrier width and  $\sigma$  is the smoothing length. In the limit  $\sigma \rightarrow 0$ , this reduces to a sharp rectangular barrier; for finite  $\sigma$ , the potential transitions smoothly between the free and barrier regions over a length scale  $\sim 3\sigma$ .

The potential is discretized into  $N$  thin slices of uniform width  $\Delta x$ , with  $N = 250$

slices used for the results presented here (convergence was verified up to  $N = 500$  with no discernible change in the results). The computational domain extends to  $x = \pm(d/2 + x_{\text{pad}})$  with  $x_{\text{pad}} = \max(5\sigma, 15 \text{ nm})$  to ensure that the potential has fully decayed to zero at the boundaries. In each slice  $j$  with local potential  $V_j = V(x_j)$ , the perpendicular wavevector  $k_{\perp}$  satisfies the quadratic equation

$$(1 - t_{\perp}^2)k_{\perp}^2 + 2t_{\perp}(t_{\parallel}k_{\parallel} - \varepsilon_j)k_{\perp} + (t_{\parallel}k_{\parallel} - \varepsilon_j)^2 - k_{\parallel}^2 = 0, \quad (7)$$

where  $\varepsilon_j = (E - V_j)/(\hbar v_{\text{F}})$  is the local dimensionless energy. The two solutions  $k_{\perp}^{(\pm)}$  correspond to right-moving and left-moving modes. The spinor ratios for each mode are  $\psi_B/\psi_A = (\varepsilon_j - t_{\perp}k_{\perp} - t_{\parallel}k_{\parallel})/(k_{\perp} - ik_{\parallel})$ . The  $2 \times 2$  spinor mode matrix  $S_j$  and propagation matrix  $P_j = \text{diag}(e^{ik_{\perp}^{(+)}\Delta x}, e^{ik_{\perp}^{(-)}\Delta x})$  are constructed for each slice, and the total transfer matrix is obtained by cascading:

$$M_{\text{total}} = \prod_{j=0}^{N-1} S_j^{-1} S_{j+1} P_{j+1}. \quad (8)$$

The complex transmission amplitude is  $t = 1/M_{\text{total},00}$  and the reflection amplitude is  $r = M_{\text{total},10}/M_{\text{total},00}$ . The computation is performed independently for each valley ( $\tau = \pm 1$ ) and each laboratory-frame transverse momentum  $k_y$ .

## Valley phase extraction and transmission-balance metric

For a carrier at laboratory-frame transverse momentum  $k_y$ , the barrier-frame conserved momentum is  $k_{\parallel}(k_y) = -\sqrt{k_{\text{F}}^2 - k_y^2} \sin \phi + k_y \cos \phi$ , where  $k_{\text{F}} = E_{\text{F}}/(\hbar v_{\text{F}})$ . The complex transmission amplitudes  $t_K$  and  $t_{K'}$  are computed independently for each valley by setting  $\tau = +1$  and  $\tau = -1$  in the tilt decomposition. The valley phase difference is

$$\Delta\delta = \arg(t_K) - \arg(t_{K'}), \quad (9)$$

wrapped to  $[-\pi, \pi]$ . The transmission-balance metric is defined as in Eq. (2). This quantity equals unity when the two valleys have identical transmission probabilities, quantifying how closely the barrier approximates a pure phase operation in the valley basis. We stress that  $\mathcal{B}$  measures only the amplitude balance of the intrinsic scattering matrix and does not account for decoherence, mode-selection imperfections, or other experimental error sources.

For the conductance polarization used in the operating regime map (Fig. 4b), the valley-resolved conductance is computed from the Landauer formula  $G_\tau = (e^2/h)(W/2\pi) \int T_\tau(k_y) dk_y$  integrated over the propagating-mode window, and the polarization is  $\mathcal{P} = (G_K - G_{K'}) / (G_K + G_{K'})$ .

### Z-X-Z Euler decomposition

Any single-qubit unitary  $U \in \text{SU}(2)$  can be decomposed as  $U(\alpha, \beta, \gamma) = R_z(\alpha) \cdot R_x(\beta) \cdot R_z(\gamma)$ , where  $R_z(\theta) = \text{diag}(e^{-i\theta/2}, e^{i\theta/2})$  and  $R_x(\theta) = \cos(\theta/2) \sigma_0 - i \sin(\theta/2) \sigma_x$  [28]. The two  $R_z$  gates are realized by smooth electrostatic barriers with independently tunable gate voltages  $V_1$  and  $V_2$ . The  $R_x(\beta)$  gate is provided by a fixed valley-mixing element that coherently couples  $|K\rangle$  and  $|K'\rangle$ ; a single fixed  $\beta$  suffices because any  $U \in \text{SU}(2)$  is reachable when  $\beta = \pi/2$  and  $\alpha, \gamma$  each span  $[0, 2\pi]$ . The Bloch-sphere coverage in Fig. 3b was computed by sweeping  $\alpha, \gamma \in [0, 2\pi]$  at  $\beta = \pi/2$  and plotting the resulting states from the input  $|K\rangle = (1, 0)^T$ .

### Device parameters and material estimates

Unless otherwise stated, the default parameters are: Fermi energy  $E_F = 100$  meV, barrier width  $d = 50$  nm, smoothing length  $\sigma = 10$  nm, barrier rotation angle  $\phi = 20^\circ$ , tilt parameter  $t = 0.5$ , and Fermi velocity  $v_F = 10^6$  m/s. The gate time is estimated as  $\tau_{\text{gate}} = d/v_F = 50$  fs, corresponding to the ballistic traversal time of the barrier region.

Valley decoherence times are estimated from the intervalley scattering rate:  $T_2 \sim \ell_{\text{iv}}/v_F$ , where  $\ell_{\text{iv}}$  is the intervalley mean free path. For clean WTe<sub>2</sub> with  $\ell_{\text{iv}} \sim 10 \mu\text{m}$  (inferred from

the long mean free paths reported in transport measurements [33, 34]), this gives  $T_2 \sim 10$  ps. These estimates should be regarded as order-of-magnitude guides; experimental determination of valley-resolved coherence times in tilted Dirac materials is an important open problem. Material-specific tilt parameters: 8-*Pmmn* borophene  $t = 0.46$  [29, 30]; WTe<sub>2</sub>  $t = 0.35$  [35, 37];  $\alpha$ -(BEDT-TTF)<sub>2</sub>I<sub>3</sub>  $t = 0.72$  [36].

## Code availability

The transfer matrix and figure generation codes are available from the corresponding author upon reasonable request.

## Data availability

All data presented in this work are generated by the computational codes described above. No experimental data were used.

## References

- [1] A. Rycerz, J. Tworzydło, and C. W. J. Beenakker, Valley filter and valley valve in graphene. *Nat. Phys.* **3**, 172 (2007).
- [2] D. Xiao, W. Yao, and Q. Niu, Valley-contrasting physics in graphene: Magnetic moment and topological transport. *Phys. Rev. Lett.* **99**, 236809 (2007).
- [3] J. R. Schaibley *et al.*, Valleytronics in 2D materials. *Nat. Rev. Mater.* **1**, 16055 (2016).
- [4] K. F. Mak, K. He, J. Shan, and T. F. Heinz, Control of valley polarization in monolayer MoS<sub>2</sub> by optical helicity. *Nat. Nanotechnol.* **7**, 494 (2012).
- [5] K. F. Mak, K. L. McGill, J. Park, and P. L. McEuen, The valley Hall effect in MoS<sub>2</sub> transistors. *Science* **344**, 1489 (2014).

- [6] C. Yesilyurt, Z. B. Siu, S. G. Tan, G. Liang, S. A. Yang, and M. B. A. Jalil, Electrically tunable valley polarization in Weyl semimetals with tilted energy dispersion. *Sci. Rep.* **9**, 4461 (2019).
- [7] S.-H. Zhang, D.-F. Shao, Z.-A. Wang, J. Yang, C.-Y. Yang, and E. Y. Tsymbal, Tunneling valley Hall effect driven by tilted Dirac fermions. *Phys. Rev. Lett.* **131**, 246301 (2023).
- [8] V. H. Nguyen and J.-C. Charlier, Klein tunneling and electron optics in Dirac-Weyl fermion systems with tilted energy dispersion. *Phys. Rev. B* **97**, 235113 (2018).
- [9] F. Zhai and K. Chang, Valley filtering in graphene with a Dirac gap. *Phys. Rev. B* **85**, 155415 (2012).
- [10] D. Moldovan, M. Ramezani Masir, L. Covaci, and F. M. Peeters, Resonant valley filtering of massive Dirac electrons. *Phys. Rev. B* **86**, 115431 (2012).
- [11] T. Fujita, M. B. A. Jalil, and S. G. Tan, Valley filter in strain engineered graphene. *Appl. Phys. Lett.* **97**, 043508 (2010).
- [12] V. M. Pereira and A. H. Castro Neto, Strain engineering of graphene's electronic structure. *Phys. Rev. Lett.* **103**, 046801 (2009).
- [13] M. Settnes, S. R. Power, M. Brandbyge, and A.-P. Jauho, Graphene nanobubbles as valley filters and beam splitters. *Phys. Rev. Lett.* **117**, 276801 (2016).
- [14] C. Yesilyurt, S. G. Tan, G. Liang, and M. B. A. Jalil, Perfect valley filter in strained graphene with single barrier region. *AIP Advances* **6**, 056303 (2016).
- [15] S. P. Milovanović, M. Ramezani Masir, and F. M. Peeters, Spin-valley filtering in strained graphene structures with artificially induced carrier mass and spin-orbit coupling. *Phys. Rev. Lett.* **113**, 046601 (2014).

- [16] J. Chen *et al.*, Room-temperature valley transistors for low-power neuromorphic computing. *Nat. Commun.* **13**, 7758 (2022).
- [17] A. Wild, R. A. Ng, M. E. Portnoi, and R. R. Hartmann, Optical valley separation in two-dimensional semimetals with tilted Dirac cones. *Sci. Rep.* **13**, 18436 (2023).
- [18] D. Gunlycke and C. T. White, Graphene valley filter using a line defect. *Phys. Rev. Lett.* **106**, 136806 (2011).
- [19] C. Yesilyurt, All-electrostatic valley filtering by barrier rotation in tilted Dirac/Weyl semimetals. *arXiv:2603.03117* (2025).
- [20] C. Yesilyurt, Z. B. Siu, S. G. Tan, G. Liang, and M. B. A. Jalil, Anomalous tunneling characteristic of Weyl semimetals with tilted energy dispersion. *Appl. Phys. Lett.* **111**, 063101 (2017).
- [21] C. Yesilyurt, Z. B. Siu, S. G. Tan, G. Liang, and M. B. A. Jalil, Conductance modulation in Weyl semimetals with tilted energy dispersion without a band gap. *J. Appl. Phys.* **121**, 244303 (2017).
- [22] M. O. Goerbig, J.-N. Fuchs, G. Montambaux, and F. Piéchon, Tilted anisotropic Dirac cones in quinoid-type graphene and  $\alpha$ -(BEDT-TTF)<sub>2</sub>I<sub>3</sub>. *Phys. Rev. B* **78**, 045415 (2008).
- [23] C. Yesilyurt, S. G. Tan, G. Liang, and M. B. A. Jalil, Klein tunneling in Weyl semimetals under the influence of magnetic field. *Sci. Rep.* **6**, 38862 (2016).
- [24] S.-H. Zhang and W. Yang, Oblique Klein tunneling in 8-*Pmmn* borophene *p-n* junctions. *Phys. Rev. B* **97**, 235440 (2018).
- [25] Z. Kong, J. Li, Y. Zhang, S.-H. Zhang, and J.-J. Zhu, Oblique and asymmetric Klein tunneling across smooth NP junctions or NPN junctions in 8-*Pmmn* borophene. *Nanomaterials* **11**, 1462 (2021).

- [26] C. Yesilyurt, Parabolic-Cylinder Approach to Valley-Polarized Conductance in Tilted Anisotropic Dirac-Weyl Systems *arXiv:2603.10490* (2026).
- [27] V. V. Cheianov and V. I. Fal'ko, Selective transmission of Dirac electrons and ballistic magnetoresistance of  $n$ - $p$  junctions in graphene. *Phys. Rev. B* **74**, 041403(R) (2006).
- [28] M. A. Nielsen and I. L. Chuang, *Quantum Computation and Quantum Information* (Cambridge University Press, 2000).
- [29] A. Lopez-Bezanilla and P. B. Littlewood, Electronic properties of 8- $Pmmn$  borophene. *Phys. Rev. B* **93**, 241405(R) (2016).
- [30] A. D. Zabolotskiy and Yu. E. Lozovik, Strain-induced pseudomagnetic field in the Dirac semimetal borophene. *Phys. Rev. B* **94**, 165403 (2016).
- [31] B. Feng *et al.*, Dirac fermions in borophene. *Phys. Rev. Lett.* **118**, 096401 (2017).
- [32] Y. Yekta, H. Hadipour, and S. A. Jafari, Tuning the tilt of the Dirac cone by atomic manipulations in 8 $Pmmn$  borophene. *Commun. Phys.* **6**, 46 (2023).
- [33] Q. Wang, C. Yesilyurt *et al.*, Anomalous photothermoelectric transport due to anisotropic energy dispersion in  $WTe_2$ . *Nano Lett.* **19**, 2647 (2019).
- [34] M. N. Ali *et al.*, Large, non-saturating magnetoresistance in  $WTe_2$ . *Nature* **514**, 205 (2014).
- [35] Y.-Y. Lv *et al.*, Experimental observation of anisotropic Adler-Bell-Jackiw anomaly in type-II Weyl semimetal  $WTe_{1.98}$  crystals at the quasiclassical regime. *Phys. Rev. Lett.* **118**, 096603 (2017).
- [36] S. Katayama, A. Kobayashi, and Y. Suzumura, Pressure-induced zero-gap semiconducting state in organic conductor  $\alpha$ -(BEDT-TTF) $_2$ I $_3$  salt. *J. Phys. Soc. Jpn.* **75**, 054705 (2006).

- [37] Y. Wang *et al.*, Gate-tunable negative longitudinal magnetoresistance in the predicted type-II Weyl semimetal WTe<sub>2</sub>. *Nat. Commun.* **7**, 13142 (2016).
- [38] J. Zheng, J. Lu, and F. Zhai, Anisotropic and gate-tunable valley filtering based on 8-*Pmmn* borophene. *Nanotechnology* **32**, 025205 (2020).
- [39] R. A. Ng, A. Wild, M. E. Portnoi, and R. R. Hartmann, Quasi-exact solutions for guided modes in two-dimensional materials with tilted Dirac cones. *Sci. Rep.* **12**, 7688 (2022).
- [40] M. A. Mojarro, R. Carrillo-Bastos, and J. A. Maytorena, Resonant transport and line-type resonances in tilted Dirac cone double-barrier structures. *arXiv:2508.17220* (2025).

## Acknowledgements

The author acknowledges the support of the Nanoelectronics Research Center (Nano Electronics Research Mühendislik Ar. Ge. Ltd. Şti., Istanbul, Turkey).

## Author contributions

C.Y. conceived the idea, developed the theoretical framework, performed all calculations, and wrote the manuscript.

## Competing interests

The author declares no competing interests.